

JAERI-Research
2000-027



JP0050456



INCIDENT-ENERGY DEPENDENCE OF THE FRAGMENTATION MECHANISM
REFLECTING THE CLUSTERING STRUCTURE OF THE ^{19}B NUCLEUS

May 2000

Hiroki TAKEMOTO, Hisashi HORIUCHI* and Akira ONO**

日本原子力研究所
Japan Atomic Energy Research Institute

本レポートは、日本原子力研究所が不定期に公刊している研究報告書です。
入手の問合わせは、日本原子力研究所研究情報部研究情報課（〒319-1195 茨城県那珂郡東海村）あて、お申し越してください。なお、このほかに財団法人原子力弘済会資料センター（〒319-1195 茨城県那珂郡東海村日本原子力研究所内）で複写による実費頒布をおこなっております。

This report is issued irregularly.

Inquiries about availability of the reports should be addressed to Research Information Division, Department of Intellectual Resources, Japan Atomic Energy Research Institute, Tokai-mura, Naka-gun, Ibaraki-ken, 319-1195, Japan.

© Japan Atomic Energy Research Institute, 2000

編集兼発行 日本原子力研究所

Incident-energy Dependence of the Fragmentation Mechanism Reflecting the Clustering Structure of the ^{19}B Nucleus

Hiroki TAKEMOTO, Hisashi HORIUCHI* and Akira ONO**

Advanced Science Research Center

(Tokai-Site)

Japan Atomic Energy Research Institute

Tokai-mura, Naka-gun, Ibaraki-ken

(Received May 10, 2000)

We investigate how clustering structure of neutron drip-line nucleus ^{19}B is reflected in heavy-ion reactions. We compare ^{19}B fragmentation in $^{19}\text{B} + ^{14}\text{N}$ reactions with ^{13}B fragmentation in $^{13}\text{B} + ^{14}\text{N}$ reactions calculated by antisymmetrized molecular dynamics, where ^{19}B has a well developed cluster structure in its ground state while ^{13}B has no clustering features in its structure. The clustering structure of the ^{19}B nucleus is reflected in its fragmentation as the simultaneous breakup of ^{19}B into He and Li isotopes, and we investigate the dependence of this cluster breakup of the ^{19}B nucleus on incident energy. We find that the most adequate incident energy for verification of the clustering structure of the ^{19}B nucleus by the use of the coincident experiment between He and Li isotopes is around 30 MeV/nucleon. This incident-energy dependence can be explained in terms of the competition between the mean-field effect and nucleon-nucleon collision processes. The mean-field effect causes the cluster breakup of the ^{19}B nucleus, while nucleon-nucleon collision processes work to destroy constituent clusters of the ^{19}B nucleus. We also investigate the influence of the neutron-rich property of the ^{19}B nucleus.

Keywords : Cluster Structure, B Isotopes, Neutron-rich Nucleus, Heavy-ion Collisions

* Department of Physics, Kyoto University

** Department of Physics, Tohoku University

中性子過剰核 ^{19}B のクラスター構造を反映したフラグメント 生成機構の入射エネルギー依存性

日本原子力研究所先端基礎研究センター
竹本 宏輝・堀内 昶*・小野 章**

(2000 年 5 月 10 日受理)

反対称化分子動力学を用いて、 $^{13}\text{B} + ^{14}\text{N}$ および $^{19}\text{B} + ^{14}\text{N}$ 反応の計算を行い、両者を比較する事により、重イオン反応における中性子過剰核 ^{19}B のクラスター構造を反映したフラグメント生成機構の研究を行った。ここで、 ^{19}B の基底状態はよく発達した He-Li クラスター構造を持ち、一方、 ^{13}B は基底状態にそのようなクラスター構造は持たない。 ^{19}B のクラスター構造は He と Li アイソトープの同時生成として、重イオン反応に反映され、その反応機構は入射エネルギー依存する。低入射エネルギーでは ^{19}B のクラスター構造が重イオン反応のフラグメント生成に反映されるが、入射エネルギーが増加するにつれ、 ^{19}B のクラスター構造はフラグメント生成には反映されなくなる。このような入射エネルギー依存性は、標的核及ぼす平均場の効果とに核子衝突の効果の競合によって説明できる。標的核からの平均場の効果は ^{19}B をクラスター崩壊させる方向に働き、二核子衝突は ^{19}B のクラスター構造を壊す方向に働く。したがって、He と Li アイソトープの同時計測により ^{19}B のクラスター構造を実験的に検証する事が可能であるが、そのための最適な入射エネルギーは $\sim 30 \text{ MeV/nucleon}$ である。また、重イオン反応における ^{19}B の中性子過剰性の影響についても調べた。

日本原子力研究所（東海駐在）：〒319-1195 茨城県那珂郡東海村白方白根 2-4

* 京都大学

** 東北大学

Contents

1. Introduction	1
2. Brief Explanation of AMD Formalism	3
3. Ground states of B Isotopes	6
4. Incident-energy Dependence of ^{19}B Fragmentation	7
5. Summary and Conclusion	23
Acknowledgments	25
References	25
Appendix	27

目 次

1. 序論	1
2. 反対称化分子動力学の概説	3
3. B アイソトープの基底状態	6
4. ^{19}B からのフラグメント生成機構の入射エネルギー依存性	7
5. まとめと結論	23
謝辞	25
参考文献	25
付録	27

This is a blank page.

1. INTRODUCTION

The amount of experimental information regarding nuclei far from the stability line has been increased greatly by means of unstable nuclear beams [1-3]. Recently obtained data of neutron-rich B isotopes display an interesting dependence of electric and magnetic moments on the neutron number N [4,5]. It is expected that the N dependence of the electromagnetic properties is caused by some structure change, such as development of cluster structure. The possibility of clustering structure in neutron-rich B isotopes has been theoretically suggested in a pioneering work with the molecular-orbital model. [6,7] In the model, B-isotope systems are described as being composed of an α - α core surrounded by neutrons and a proton. It was found that the optimum distance of the α - α core of the B isotope became larger with an increase in the neutron number N in the $N > 8$ region.

Recently, structure of odd-even B isotopes up to the neutron drip-line was studied systematically with antisymmetrized molecular dynamics (AMD) [8]. The AMD method is free from any model assumptions such as the existence of clusters, so it is appropriate for studying the neutron-number dependence of the structure, such as the structure change from shell-model-like structure to clustering structure. Binding energy and other observed data of B isotopes are reproduced by the AMD method quite well, and, in particular, a very good reproduction of electromagnetic properties is obtained. The behavior of electromagnetic properties has been explained in terms of the drastic structure change from the shell-model-like structure to the clustering structure; namely, the neutron-closed shell nucleus, the ^{13}B nucleus, possesses the shell-model-like structure, and the cluster structure develops with an increase of N beyond $N = 8$. This explanation gives us an important indication that the clustering structure in neutron-rich B nuclei is strongly suggested by experimental data.

In this paper we investigate by using the AMD method how the well developed cluster structure of the ^{19}B nucleus predicted theoretically is reflected in heavy-ion reactions, and suggest the experimental way to verify the cluster structure of the ^{19}B nucleus by the use of the fragmentation reaction. In order to study this kind of subject on the reflection of

nuclear structure in heavy-ion reactions, the theory needs to describe both nuclear structure and nuclear reaction. The AMD method is this kind of theory. The AMD method does not assume any reaction mechanisms producing fragments such as a coalescence, the participant-spectator mechanism, neck fragmentation, bubble fragmentation, the liquid-vapor phase transition, and so on [14]. Therefore we can study these various kinds of fragmentation mechanisms systematically, and we can also study an unknown reaction mechanism. Furthermore the AMD method is applicable not only to nuclear reaction problems [10–13] but also to nuclear structure problems [8,9] where the AMD method does not set any structural assumption, and can describe the mean-field character and the clustering degrees of freedom. Hence, by using the AMD method, we can study the fragmentation related to nuclear structure [15,16] such as the cluster structure of the ^{19}B nucleus.

Recently we have investigated the fragmentation mechanism reflecting the cluster structure of the ^{19}B nucleus by calculating $^{19}\text{B} + ^{14}\text{N}$ and $^{13}\text{B} + ^{14}\text{N}$ reactions at 35 MeV/nucleon with the AMD method [17]. Here the ^{19}B nucleus has the well developed cluster structure, while the ^{13}B nucleus has the shell-model-like structure having no seed of clusters. By comparing ^{19}B fragmentation with ^{13}B fragmentation, we have found that more He and Li isotopes are produced in ^{19}B fragmentation than in ^{13}B fragmentation, and that most of He and Li isotopes arising from ^{19}B fragmentation are produced simultaneously. From this result, we have concluded that the cluster structure of the ^{19}B nucleus is reflected as the simultaneous breakup of the ^{19}B nucleus into He and Li isotopes in its fragmentation, and we have suggested that there is the possibility that the clustering structure of the ^{19}B nucleus in its ground state can be verified experimentally by the use of ^{19}B fragmentation in heavy-ion reactions, in particular, in a coincident experiment between He and Li isotopes. It has not been yet confirmed experimentally whether the ^{19}B nucleus has the cluster structure or not.

In this paper, we calculate $^{19}\text{B} + ^{14}\text{N}$ and $^{13}\text{B} + ^{14}\text{N}$ reactions at several incident energy by using the AMD method, and investigate the incident-energy dependence of ^{19}B fragmentation to search for the most suitable incident energy to verify the cluster

structure of the ^{19}B nucleus experimentally by the use of the fragmentation mechanism. Furthermore we also study the reaction mechanism reflecting the neutron-rich property of the ^{19}B nucleus. In the next section, we describe the AMD formalism briefly. The properties of the ground states of B isotopes calculated in the AMD framework are given in Sec. 3. In Sec. 4 A we give the general feature of ^{19}B fragmentation, and in Sec. 4 B we make an investigation into the incident-energy dependence of the fragmentation mechanism reflecting the cluster structure of the ^{19}B nucleus, and we make clear the effect of mean-field and nucleon-nucleon collision processes on the cluster breakup of ^{19}B in Sec. 4 C. In Sec. 4 D we describe the reaction mechanism reflecting the neutron-rich property of the ^{19}B nucleus. Finally, we close the paper by giving a summary and conclusions in Sec. 5.

2. BRIEF EXPLANATION OF AMD FORMALISM

The formalism of AMD is described in detail in Ref. [10], and we give only an outline of the AMD method below. In AMD, the wave function of the A -nucleon system $|\Phi\rangle$ is described by a Slater determinant,

$$|\Phi\rangle = \frac{1}{\sqrt{A!}} \det [\varphi_i(j)], \quad (1)$$

where

$$\varphi_i = \phi_{\mathbf{z}_i} \chi_{\alpha_i} \quad (\alpha_i = p \uparrow, p \downarrow, n \uparrow, n \downarrow) \quad (2)$$

and

$$\phi_{\mathbf{z}_i} = \left(\frac{2\nu}{\pi}\right)^{\frac{3}{4}} \exp \left[-\nu \left(\mathbf{r} - \frac{\mathbf{Z}_i}{\sqrt{\nu}} \right)^2 + \frac{1}{2} \mathbf{Z}_i^2 \right], \quad (3)$$

$$\mathbf{Z}_i = \sqrt{\nu} \mathbf{D}_i + \frac{i}{2\hbar\sqrt{\nu}} \mathbf{K}_i \quad (4)$$

Here, χ_{α_i} and $\phi_{\mathbf{z}_i}$ represent the spin-isospin wave function and the spatial wave function of the i th single particle state, respectively. ν is the width parameter, which is independent

of time, and we use $\nu = 0.16 \text{ fm}^{-2}$ in the following calculations. $Z = \{\mathbf{Z}_i\}$ represent the positions of the centers of Gaussians, and the A -body wave function $|\Phi\rangle$ is parameterized by Z .

The time development of Z is determined by the time-dependent variational principle, which leads to the following equation of motion for Z :

$$i\hbar \sum_{j\tau} C_{i\sigma,j\tau} \frac{d}{dt} Z_{j\tau} = \frac{\partial \mathcal{H}}{\partial Z_{i\sigma}^*} \text{ and c.c.}, \quad (5)$$

$$\mathcal{H}(Z, Z^*) = \frac{\langle \Phi(Z) | H | \Phi(Z) \rangle}{\langle \Phi(Z) | \Phi(Z) \rangle} - \frac{3\hbar^2 \nu}{2M} A + T_0(A - N_F). \quad (6)$$

$$C_{i\sigma,j\tau} = \frac{\partial^2}{\partial Z_{i\sigma}^* \partial Z_{j\tau}} \ln \langle \Phi(Z) | \Phi(Z) \rangle, \quad (7)$$

where $\sigma, \tau = x, y, z$. In this paper we adopted the Gogny force [18] as the effective central force in the Hamiltonian. The Gogny force contains a finite range two-body force and a density-dependent zero-range repulsive force, and it gives a momentum-dependent mean field. The second and third terms in Eq. (6) are correction for the sake of removing the zero-point energies of the center-of-mass motion of fragments in the Hamiltonian \mathcal{H} . Without this correction, we can not reproduce Q -values in treating fragment formation. N_F represents the number of fragments, and is a function of real parts of Z (see appendix A). The value of T_0 should be equal to that of $3\hbar^2 \nu / 2M$ in principal, but it is slightly changed in order to obtain better binding energies of nuclei. In this paper T_0 is set to be 8.8 MeV.

When we apply AMD to heavy ion reactions, nucleon-nucleon collision processes should be incorporated. In the AMD framework, two nucleons scatter stochastically when the spatial distance between them is small. But due to the effect of antisymmetrization, the centers of Gaussians Z , $\{\mathbf{D}_i\}$ and $\{\mathbf{K}_i\}$, do not always have the meaning of positions and momenta of nucleons. Hence we must transform coordinates Z to the physical coordinates $W = \{\mathbf{W}_i\}$, whose real and imaginary parts can be interpreted as the positions and momenta of nucleons, respectively:

$$\mathbf{W}_i = \sum_{j=1}^A \left(\sqrt{Q} \right)_{ij} \mathbf{Z}_j = \sqrt{\nu} \mathbf{R}_i + \frac{i}{2h\sqrt{\nu}} \mathbf{P}_i, \quad (8)$$

where

$$Q_{ij} = \frac{\partial}{\partial (\mathbf{Z}_i^* \cdot \mathbf{Z}_j)} \ln \langle \Phi(Z) | \Phi(Z) \rangle. \quad (9)$$

In the AMD framework, when the physical positions \mathbf{R}_i and \mathbf{R}_j of two nucleons become close, nucleon-nucleon collision can occur and the physical momenta \mathbf{P}_i and \mathbf{P}_j are changed stochastically into \mathbf{P}'_i and \mathbf{P}'_j ; namely, $W = \{\mathbf{W}_i\}$ changes into $W' = \{\mathbf{W}'_i\}$ (see appendix B about nucleon-nucleon cross sections used here). Since we have to calculate the time development of Z after the nucleon-nucleon collision has occurred, we must retransform W' to Z' . But it can happen that there exist no coordinates Z' corresponding to W' . If this situation occurs, this nucleon-nucleon collision is not realized. We refer to those W' which have no corresponding Z' as Pauli forbidden and others as Pauli allowed. The above definition of the Pauli forbidden and allowed regions is the extension of that of the time-dependent cluster model [19]. In the AMD method, the fermionic nature of nucleons is treated exactly, because the wave function of an A -body system is antisymmetrized by a Slater determinant. Hence the Pauli principle is fully incorporated.

Ground states of colliding nuclei have to be prepared before AMD simulations. In order to construct the wave function for the ground state, we should determine the parameters Z which minimize the expectation value of the Hamiltonian \mathcal{H} . First, we randomly choose Z , which expresses an initial state with high excitation energy. This initial state is then cooled down by applying the frictional cooling equations for Z , which are obtained by multiplying the right-hand side of Eq. (5) with $(\lambda + i\mu)$:

$$i\hbar \sum_{j\tau} C_{i\sigma,j\tau} \frac{d}{dt} Z_{j\tau} = (\lambda + i\mu) \frac{\partial \mathcal{H}}{\partial Z_{i\sigma}^*} \text{ and c.c.}, \quad (10)$$

where λ and μ are arbitrary real numbers. It is easily proved that energy of a system decreases with time,

$$\frac{d\mathcal{H}}{dt} < 0, \quad (11)$$

if $\mu < 0$. Then the wave function of the minimum-energy state is obtained after sufficient cooling time. This cooling method explained above is called the frictional cooling method [9].

3. GROUND STATES OF B ISOTOPES

Before turning to the main subject, a few remarks should be made concerning the properties of B isotopes obtained by the frictional cooling method. Density distributions of B isotopes based on the AMD wave functions obtained by the frictional cooling method are displayed in Fig. 1. AMD calculations show the development of the cluster structure of B isotopes with an increase of the neutron number; namely, the ^{13}B nucleus which is a neutron closed shell nucleus has the shell-model-like spherical structure, and gradually the cluster structure develops as the neutron number increases, and the ^{19}B nucleus which is a neutron-drip-line nucleus has the well developed cluster structure. This development of the clustering structure of B isotopes with increasing neutron number is considered to be a unique structure in unstable neutron-rich nuclei to bind neutrons as many as possible by a few protons. Such a clustering structure of neutron-rich nuclei has not been confirmed experimentally.

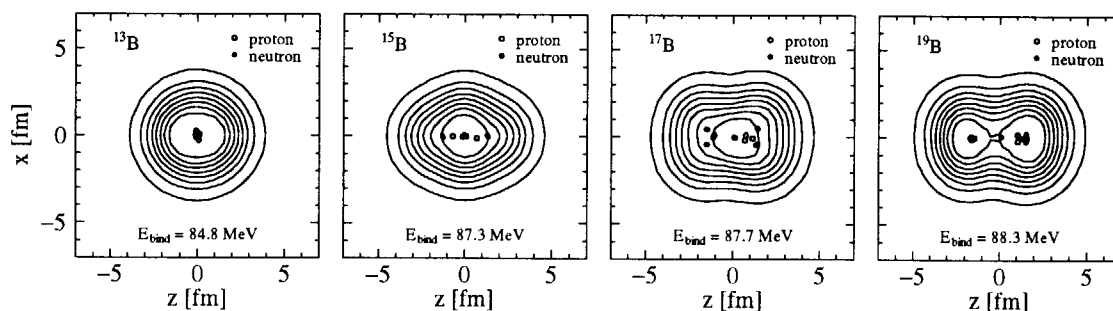


FIG. 1. Density distributions of the ground states of B isotopes based on the AMD wave functions obtained by the frictional cooling method. Open and filled circles represent the centers of Gaussians of protons and neutrons, respectively.

Figure 2 compares the binding energies and root-mean-square radii of the ground states

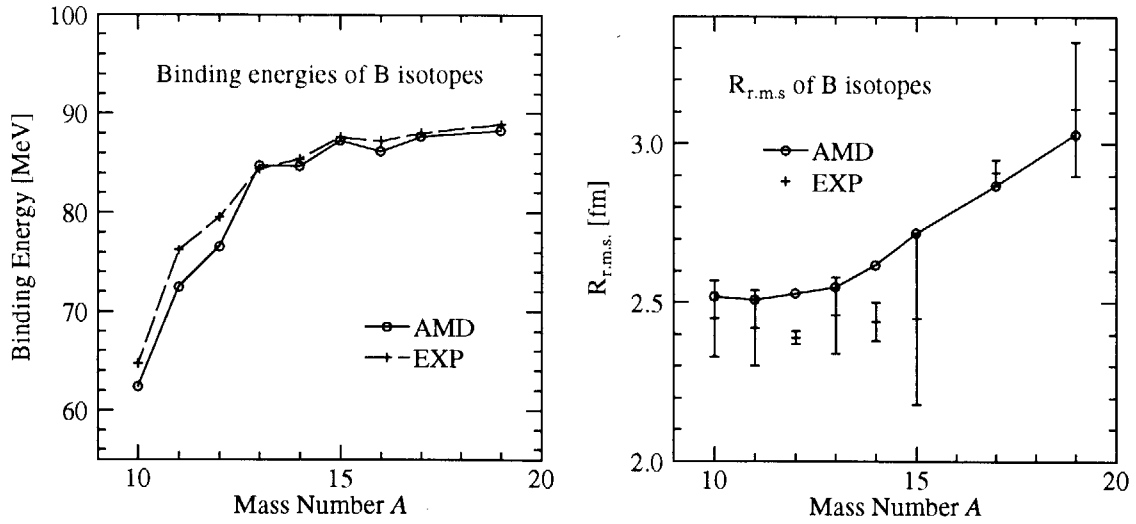


FIG. 2. Binding energies and root-mean-square radii of the ground states of B isotopes, which are shown in left and right panels, respectively. The solid and dashed lines indicate the AMD calculation and experimental data, respectively.

of B isotopes calculated by the AMD method with those of the experimental data, which are shown in left and right panels, respectively. The binding energies of B isotopes within the AMD framework reproduce the experimental data quite well. It should be stressed here that relative binding energy (Q value) are important to describe fragmentation in heavy-ion reactions. Experimental data for root-mean-square radii of B isotopes are also reproduced quite well by the AMD calculations. The root-mean-square radii become large with the increase of the neutron number N due to the development of the cluster structure with the increase of N , as is shown in Fig. 1.

4. INCIDENT-ENERGY DEPENDENCE OF ^{19}B FRAGMENTATION

We investigate the incident-energy dependence of the fragmentation mechanism reflecting the cluster structure of the ^{19}B nucleus in its ground state, and search for the most adequate incident-energy region to verify the cluster structure of the ^{19}B nucleus experimentally by the use of the fragmentation reactions. We also study the reaction

mechanism arising from the neutron-rich property of the ^{19}B nucleus. We calculate ^{13}B and ^{19}B induced reactions on the ^{14}N target at several incident energies by using the AMD method, and compare ^{19}B fragmentation with ^{13}B fragmentation where the ^{19}B nucleus has the well developed cluster structure, while the ^{13}B nucleus has no seed of clusters in the ground state, as is shown in Fig. 1.

The analyses in this paper are done for the projectile-like fragments, namely the fragments from ^{13}B and ^{19}B nuclei. In order to separate projectile-like and target-like fragments, we give the following definition. The fragments emitted in the *forward* direction are considered to be target-like fragments, while the fragments emitted in the *backward* direction are considered to be projectile-like fragments. We distinguish the *forward* and *backward* directions based on the nucleon-nucleon center-of-mass system, that is to say, the fragments whose P_z/A (the incident direction is the z direction) is larger than that of the nucleon-nucleon center-of-mass system are considered to be scattered in the *forward* direction, and the fragments whose P_z/A is smaller than that of nucleon-nucleon center-of-mass system are considered to be scattered *backward* direction.

P_z/A distributions of He isotope produced in $^{19}\text{B} + ^{14}\text{N}$ (left panels) and $^{13}\text{B} + ^{14}\text{N}$ (right panels) at 25, 35, and 55 MeV/nucleon are shown in Fig 3 from top to bottom panels. In all panels, left and right arrows indicate the incident momenta of the projectile which is ^{19}B or ^{13}B in this case and the target which is ^{14}N , respectively. The central arrows inscribed ‘cut off’ indicate momenta of nucleon-nucleon center-of-mass systems in the center-of-mass systems where AMD calculations are performed. The projectile-like and target-like peaks are clearly seen in P_z/A distributions when the incident energy is beyond 35 MeV/nucleon, and we see that our definition of the separation of projectile-like and target-like fragments works well. However there are not seen two peaks definitely in P_z distributions at 25 MeV/nucleon because projectile-like and target-like peaks overlap each other. Accordingly, our definition of projectile-like and target-like fragments does not work well in the low incident energy region. But we can extract projectile-like fragments by coincidence with another projectile-like fragments, which is shown by dashed lines that indicate P_z/A distributions of He isotopes in coincidence with projectile-like Li isotopes.

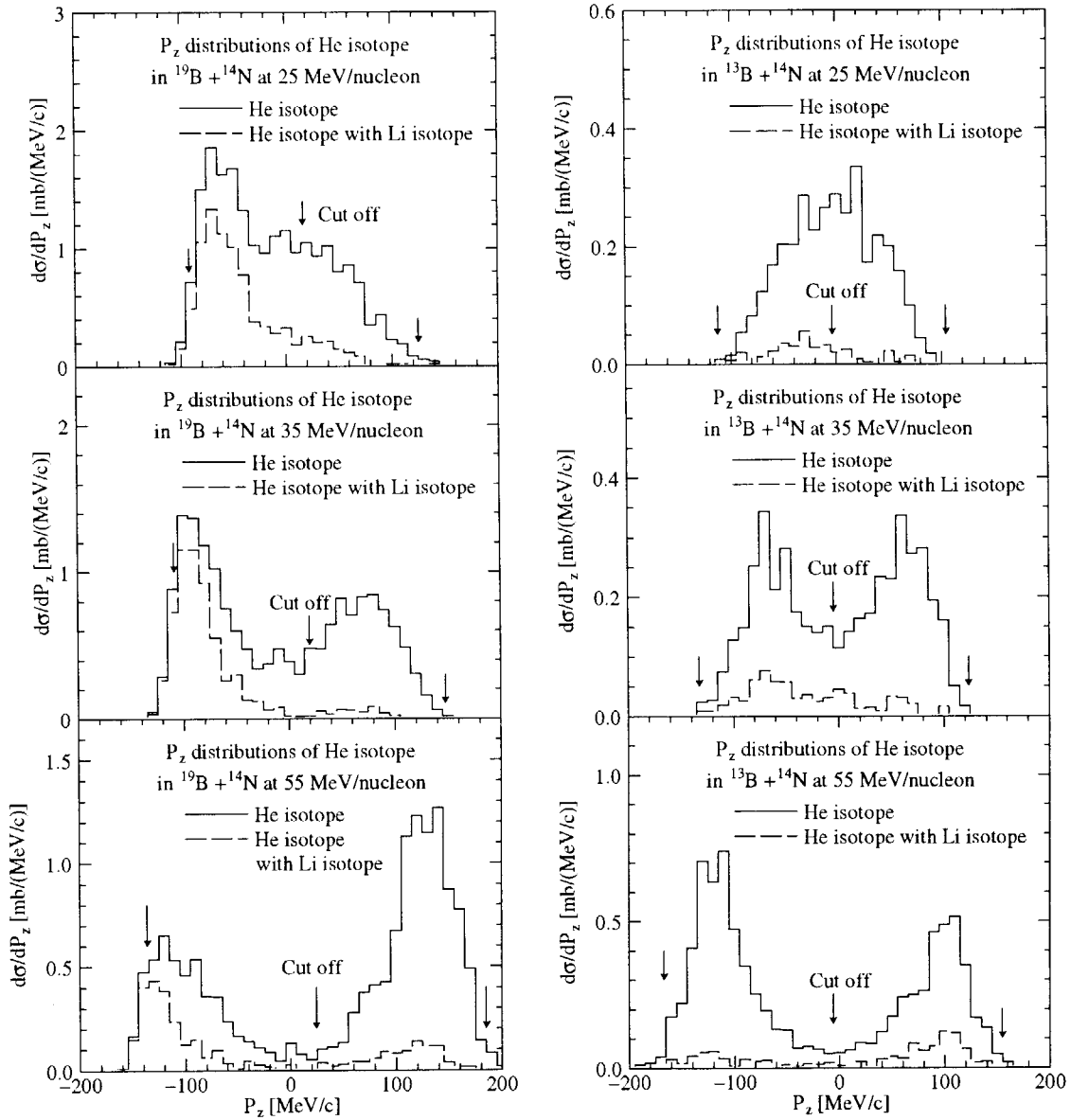


FIG. 3. P_z/A distributions of the He isotope in $^{19}\text{B} + ^{14}\text{N}$ (left panels) and $^{13}\text{B} + ^{14}\text{N}$ (right panels) at 25 (top panels), 35 (middle panels) and 55 (bottom panels) MeV/nucleon. Left and right arrows indicate the incident momenta of the projectile, which is ^{19}B or ^{13}B in these calculations, and the target, which is ^{14}N in this case, respectively, and center arrows inscribed 'cut off' indicate momenta of nucleon-nucleon center-of-mass systems in the center-of-mass systems where AMD simulations are performed. Broken lines show P_z/A distributions in coincidence with projectile-like Li isotopes.

By taking a coincidence with projectile-like Li isotopes, projectile-like peaks appear in P_z/A distributions of the He isotope even if the incident energy is low. At 55 MeV/nucleon, the target-like peak also comes to appear in the coincident P_z/A distribution. This is because the system breaks up into more small pieces when the incident energy becomes higher.

A. Features of fragmentation mechanisms reflecting the difference in character between ^{13}B and ^{19}B nuclei

As a beginning, we show how the difference in character between the ^{19}B and ^{13}B nuclei is reflected in their fragmentation. The left panel of Fig. 4 compares a charge distribution from ^{19}B fragmentation with that from ^{13}B fragmentation in ^{14}N -target reactions at 35 MeV/nucleon. Solid and broken lines indicate the charge distributions from ^{19}B and ^{13}B fragmentation, respectively. We can see three distinct features reflecting the difference in character between the ^{13}B and ^{19}B nuclei in charge distributions [17]. First one is the reflection of cluster structure of the ^{19}B nuclei; namely, more He and Li isotopes are produced in ^{19}B fragmentation than in ^{13}B fragmentation. Second one is the reflection of the neutron-rich property of the ^{19}B nucleus, which is shown by the abundance of fragments with $Z > 5$ in ^{19}B fragmentation compared with in ^{13}B fragmentation. This is because the ^{19}B nucleus approaches the stability line by exchanging neutrons with protons. The neutron-rich property of the ^{19}B nucleus is also reflected as the suppression of the production of Be isotopes in ^{19}B fragmentation compared with ^{13}B fragmentation. This is due to the opposite reason causing the abundance of the fragments with $Z > 5$ in ^{19}B fragmentation. Third one is the reflection of a loosely bound system of the ^{19}B nucleus with respect to the neutron emission. This is indicated by the production cross section of B isotopes from which the contribution of elastic and inelastic scattering is excluded. Neutron evaporation from the ^{19}B nucleus is more preferable than that from the ^{13}B nucleus since the production cross section of B isotopes in the ^{19}B induced reaction is larger than that in the ^{13}B induced one.

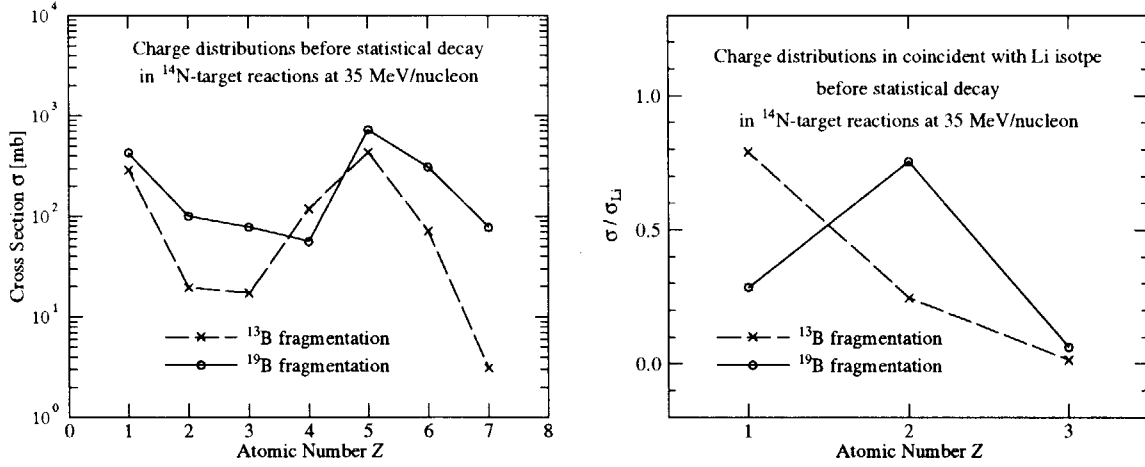


FIG. 4. Charge distributions and coincident charge distributions with the projectile-like Li isotope from ^{13}B and ^{19}B fragmentation in ^{14}N -target reactions at 35 MeV/nucleon, which are shown in upper and lower panels, respectively. Solid and broken lines indicate those from ^{19}B and ^{13}B fragmentation, respectively.

If the abundance of He and Li isotopes in ^{19}B fragmentation compared with in ^{13}B fragmentation is caused by the cluster structure of the ^{19}B nucleus, these He and Li isotopes should be produced simultaneously. The right panel of Fig. 4 displays charge distributions in coincidence with the projectile-like Li isotope where the coincident cross sections are normalized by the total production cross section of Li isotopes. Solid and broken lines indicate those from ^{19}B and ^{13}B fragmentation, respectively. As is clearly seen, most of Li isotopes are produced by the simultaneous breakup of the ^{19}B nucleus into He and Li isotopes in ^{19}B fragmentation, while most of Li isotopes are accompanied with the emission of H isotopes in ^{13}B fragmentation. From the above result, we conclude that the cluster structure of the ^{19}B nucleus is reflected as the simultaneous breakup into He and Li isotopes in ^{19}B fragmentation, and suggest that there is a possibility to verify the cluster structure of the ^{19}B nucleus by the coincident experiment between He and Li isotopes in ^{19}B fragmentation [17].

Having obtained a general view of ^{13}B and ^{19}B fragmentation, we may turn to the incident-energy dependence of ^{13}B and ^{19}B fragmentation. Left and right panels of Fig. 5

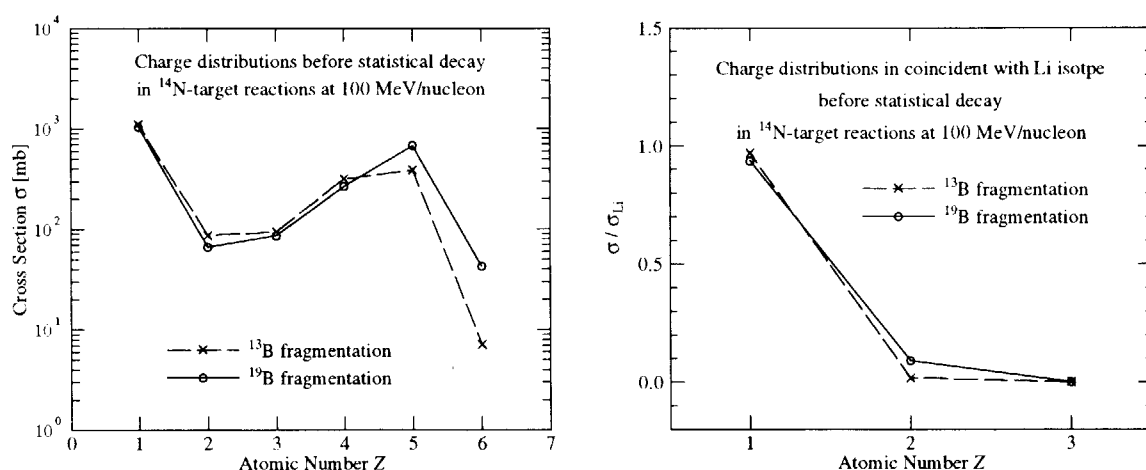


FIG. 5. Charge distributions and coincident charge distributions with the projectile-like Li isotope from ^{13}B and ^{19}B fragmentation in ^{14}N -target reactions at 100 MeV/nucleon, which are shown in upper and lower panels, respectively. Solid and broken lines indicate those from ^{19}B and ^{13}B fragmentation, respectively.

show charge and coincident charge distributions at 100 MeV/nucleon, respectively. As is shown in the upper panel of Fig. 5, charge distributions from ^{19}B and ^{13}B fragmentation become very similar each other when the incident energy is increased up to 100 MeV/nucleon. Especially, the production cross sections of He and Li isotopes are almost same, and Li isotopes are produced by the reaction accompanied with the emission of H isotopes in both fragmentation, as is shown in the coincident charge distributions with the projectile-like Li isotope. This results indicates that the clustering structure of the ^{19}B nucleus is not reflected in high incident-energy region. Concerning the reflections of the neutron-rich property and the neutron-loosely-bound system of the ^{19}B nucleus, they slightly remain at 100 MeV/nucleon, which is shown by the slight abundance of fragments with $Z \geq 5$ in ^{19}B fragmentation compared with in ^{13}B fragmentation.

B. Fragmentation mechanism reflecting the cluster structure of the ^{19}B nucleus

Hereafter we shall focus on the fragmentation mechanisms reflecting the cluster structure of the ^{19}B nucleus in view of the production of Li isotopes. The left upper panel of Fig. 6 shows excitation functions of Li isotopes in $^{13}\text{B} + ^{14}\text{N}$ and $^{19}\text{B} + ^{14}\text{N}$ reactions. At 25 MeV/nucleon, the production cross section of Li isotopes in ^{19}B fragmentation is much larger than that in ^{13}B fragmentation. As the incident energy increases up to 55 MeV/nucleon, the production cross sections of Li isotopes in ^{19}B fragmentation decreases, while that in ^{13}B fragmentation increases, and they meet at 55 MeV/nucleon. As incident energy increases further, these two cross sections rise slowly each together, that is to say, the difference between ^{19}B and ^{13}B fragmentation disappears in high incident-energy region above 55 MeV/nucleon.

As has been pointed out, the cluster structure of the ^{19}B nucleus is reflected as the simultaneous breakup of the ^{19}B nucleus into He and Li isotopes. The right upper panel of Fig. 6 shows coincident cross sections of Li isotopes with H or He isotopes extracted from the production cross sections of Li isotopes in $^{19}\text{B} + ^{14}\text{N}$ reactions, which are indicated by dotted and dotted-dashed lines, respectively. The coincident cross section between He and Li isotopes in ^{19}B fragmentation decrease monotonously with the incident energy increasing, and, on the other hand, the coincident cross section between H and Li isotopes increases with the incident energy increasing. These two coincident cross sections cross around 50 MeV/nucleon, and the dominant process producing Li isotopes in ^{19}B fragmentation turns from the simultaneous breakup into He and Li isotopes in low incident energies to the breakup of ^{19}B into the Li isotope accompanied with H isotopes in high incident energies. By comparing the coincident cross section of Li isotopes with H isotopes in ^{19}B fragmentation with the production cross section of Li isotopes in ^{13}B fragmentation where the dominant process producing Li isotopes is the breakup of ^{13}B into a Li isotope accompanied with H isotopes, we see that both cross sections have the similar incident-energy dependence, and absolute values of cross sections are almost the same each other in the whole incident energy region except for 25 MeV/nucleon.

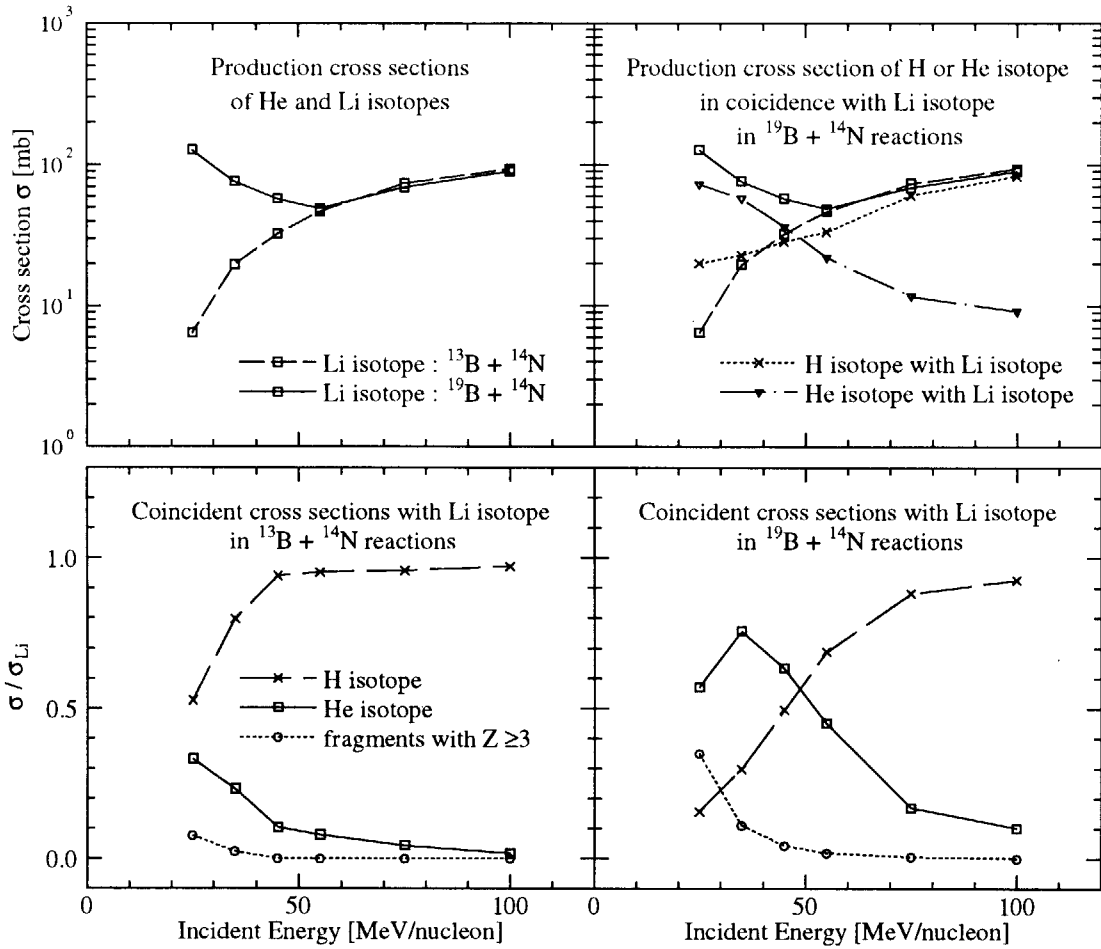


FIG. 6. Excitation functions of Li isotope productions in $^{19}\text{B} + ^{14}\text{N}$ and $^{13}\text{B} + ^{14}\text{N}$ reactions, which are indicated by solid and broken lines, respectively, in the left upper panel. In the right top panel, coincident cross sections of Li isotope with He and H isotopes in ^{19}B induced reactions are shown by dotted-dashed and dotted lines, respectively. Left and right lower panels show the ratios of the coincident cross sections of a Li isotope with H and He isotopes and fragments with $Z \geq 3$ to total production cross sections of Li isotopes in $^{13}\text{B} + ^{14}\text{N}$ and $^{19}\text{B} + ^{14}\text{N}$ reactions, respectively. Solid, broken and dotted lines indicate those in coincidence with H and He isotopes, and fragments with $Z \geq 3$, respectively.

Accordingly we find that the abundance of Li isotopes in ^{19}B fragmentation compared with ^{13}B fragmentation in low-incident energy region is due to the simultaneous breakup of the ^{19}B nucleus into He and Li isotopes by reflecting the cluster structure of the ^{19}B nucleus, and that at high incident-energy the dominant process producing Li isotopes becomes the breakup into a Li isotope accompanied with H isotopes in both ^{19}B and ^{13}B fragmentation, and therefore the difference of structure between ^{13}B and ^{19}B nuclei is not seen in their fragmentation at high incident energy.

In order to see the change of reaction mechanisms producing Li isotopes in ^{19}B and ^{13}B fragmentation, we plot the ratio of coincident cross sections of Li isotopes with H or He isotopes or fragments with $Z \geq 3$ to total production cross sections of Li isotopes, which are indicated by solid, broken and dotted lines in lower panels of Fig. 6, as a function of the incident energy. Left and right lower panels of Fig. 6 show ^{13}B and ^{19}B fragmentation, respectively. In the case of ^{13}B fragmentation, the dominant process producing Li isotopes is the breakup into a Li isotope and H isotopes in whole incident energy region investigated here. Namely, there is scarcely any correlation among production of He and Li isotopes in ^{13}B fragmentation at all incident energy because the ^{13}B nucleus has no seed of clusters in its ground state. On the other hand, in the case of ^{19}B fragmentation, the dominant process producing Li isotopes is the simultaneous breakup of the ^{19}B nucleus into He and Li isotopes in low incident-energy region. The contribution of this cluster breakup of the ^{19}B nucleus to the production of Li isotopes has the peak at ~ 35 MeV/nucleon, and its ratio to the production of Li isotopes reaches to 80 percent by reflecting the cluster structure of the ^{19}B nucleus.

The contribution of the cluster breakup of the ^{19}B nucleus becomes small with the incident energy increasing, and above ~ 50 MeV/nucleon the dominant process producing Li isotopes turns to the breakup mechanism accompanied with H isotopes from the cluster breakup of the ^{19}B nucleus. This means that the information of cluster structure of the ^{19}B nucleus loses in its fragmentation at high incident energy due to more violent collisions. In the lower incident-energy region below 35 MeV/nucleon, the contribution of the cluster breakup of the ^{19}B nucleus to the production of Li isotopes decreases. This is because the

breakup of the ^{19}B nucleus accompanied with proton transfer reactions contaminates the cluster breakup of the ^{19}B nucleus into He and Li isotopes in heavy-ion reactions at lower incident energy due to the neutron-rich property of the ^{19}B nucleus, which is indicated by the dotted line that represents the ratio of the coincident cross section between a Li isotope and the fragment with $Z \geq 3$ to the total cross section of Li isotopes in the right bottom panel of Fig. 6. By comparing ^{13}B fragmentation with ^{19}B fragmentation, the ratio of the breakup of the ^{19}B nucleus accompanied with proton transfer to the total production cross section of Li isotopes reaches up to 35 % at 25 MeV/nucleon, and, on the other hand, this ratio in ^{13}B fragmentation at 25 MeV/nucleon reaches up to less than 10 %.

These results lead to the following conclusions. The cluster structure of the ^{19}B nucleus is reflected as the simultaneous breakup of the ^{19}B nucleus into He and Li isotopes in its fragmentation. The contribution of the cluster breakup of the ^{19}B nucleus to the production of Li isotopes becomes largest around Fermi energy. In higher incident energy region, the cluster structure of the ^{19}B nucleus is not reflected in its fragmentation due to more violent collisions, and in lower incident energy region, the cluster breakup of the ^{19}B nucleus is contaminated by proton transfer reactions due to the neutron-rich property of the ^{19}B nucleus. Therefore we suggest here that coincident experiment between He and Li isotopes may confirm whether the ^{19}B nucleus has cluster structure in its ground state or not, and that the adequate incident energy for the experiment is around 30 MeV/nucleon.

C. Effect of mean field and nucleon-nucleon collision processes on the cluster breakup of the ^{19}B nucleus

Let us consider the incident-energy dependence of the fragmentation mechanism reflecting the cluster structure of the ^{19}B nucleus from the point of view of the competition between mean field effect and nucleon-nucleon collision processes. In order to extract the mean-field effect in the AMD framework, we perform AMD simulations switching off nucleon-nucleon collision processes.

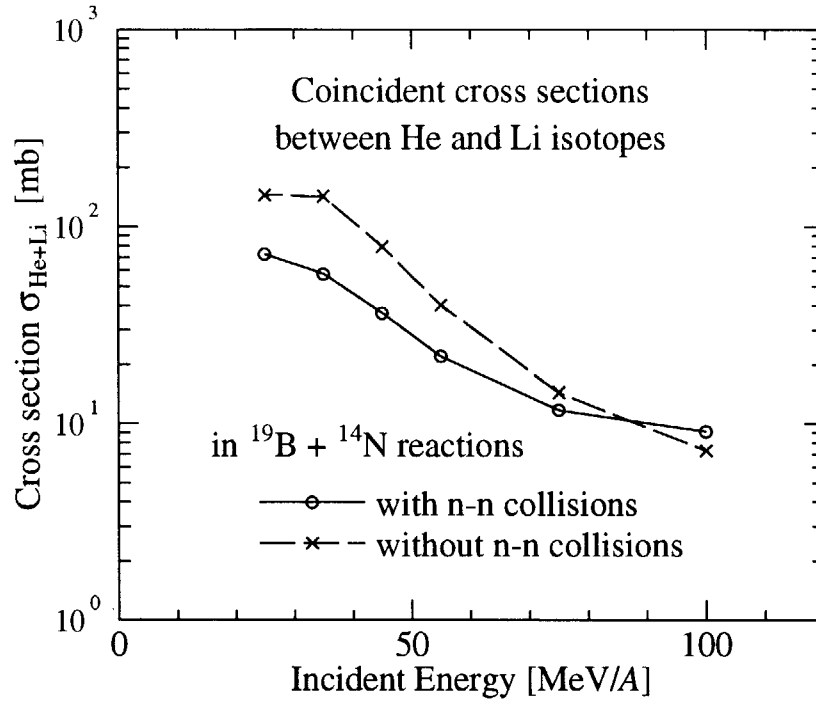


FIG. 7. Incident-energy dependence of coincident cross sections between He and Li isotopes in $^{19}\text{B} + ^{14}\text{N}$ reactions with and without nucleon-nucleon collision processes, which are indicated by solid and broken lines, respectively.

Figure 7 compares the coincident cross sections between He and Li isotopes in $^{19}\text{B} + ^{14}\text{N}$ reactions with and without nucleon-nucleon collisions, which are indicated by solid and broken lines, respectively. In low incident-energy region the cross section of the cluster breakup of the ^{19}B nucleus into He and Li isotopes in the case without nucleon-nucleon collisions is much larger than that in the case with nucleon-nucleon collision processes; namely, the cross section of the cluster breakup of the ^{19}B nucleus is reduced by nucleon-nucleon collision processes. Thus we see that the mean field from the ^{14}N target mainly causes the cluster breakup of the ^{19}B nucleus into He and Li isotopes, and that nucleon-nucleon collision processes work to destroy constituent clusters of the ^{19}B nucleus.

As the incident energy is increasing, the cross section of the cluster breakup of the ^{19}B

nucleus decreases monotonously, and the tendency of this decrease with the incident energy increasing remains even if nucleon-nucleon collision processes are included. Therefore we can see that the incident-energy dependence of the cluster breakup of the ^{19}B nucleus is mainly determined by the mean-field effect from the target. The effect of the mean-field from the target becomes weak with the incident energy increasing because the interaction time becomes short, and, as a result, the ^{19}B nucleus cannot get the perturbation from the target enough to break up into He and Li clusters in high incident-energy region.

For the moment let us look closely at the effect of the mean field and the nucleon-nucleon collisions on the cluster breakup of the ^{19}B nucleus in terms of the impact-parameter dependence. Left and right upper panels of Fig. 8 show the impact-parameter dependence of Li production in $^{19}\text{B} + ^{14}\text{N}$ reactions at 35 and 100 MeV/nucleon, respectively, and bottom panels show the number of nucleon-nucleon collisions per event as a function of the impact parameter. Solid and broken lines indicate the cases with and without nucleon-nucleon collisions, respectively, and dotted lines indicate the impact parameter dependence of the cluster breakup into Li and He isotopes with inclusion of nucleon-nucleon collision processes. It should be noticed here that all Li isotopes are produced together with He isotopes in the case without nucleon-nucleon collision processes.

At 35 MeV/nucleon, the cluster breakup of the ^{19}B nucleus only by the mean-field effect occurs most frequently at semi-peripheral collisions around 3–5 fm. It is considered that adequate perturbation by the mean field from the target is necessary for the ^{19}B nucleus to break up into He and Li isotopes. This peak around 3–5 fm arising from the mean-field effect disappears with inclusion of nucleon-nucleon collisions. As is shown in bottom panels of Fig. 8, more nucleon-nucleon collision processes occur at more central collisions. As a result, in the *real* $^{19}\text{B} + ^{14}\text{N}$ reaction at 35 MeV/nucleon, the ^{19}B nucleus breaks up into He and Li isotopes at peripheral collisions most frequently, and the probability of the cluster breakup of the ^{19}B nucleus decreases with the impact parameter decreasing.

When incident energy increases up to 100 MeV/nucleon, the peak arising from the mean-field effect shifts to central collisions from semi-peripheral collisions, and the height of the peak becomes lower. This is because the interaction time becomes short with the in-

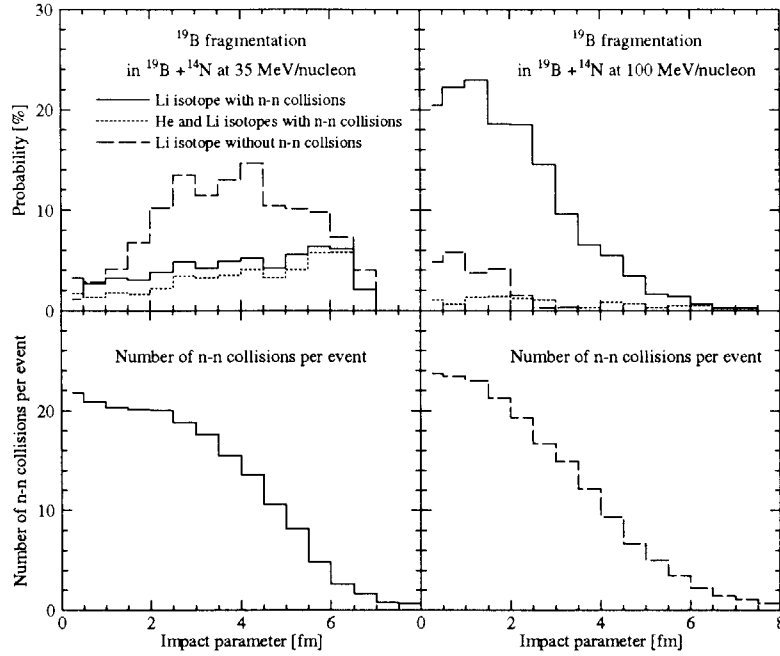


FIG. 8. Impact-parameter dependence of the production of Li isotopes in $^{19}\text{B} + ^{14}\text{N}$ reactions at 35 and 100 MeV/nucleon, which are shown in left and right top panels, respectively. Solid and broken lines indicate the cases with and without nucleon-nucleon collision processes, respectively. Dotted lines represent the impact-parameter dependence of the cluster breakup of the ^{19}B nucleus into He and Li isotopes in the cases with nucleon-nucleon collision processes. Left and right bottom panels show number of nucleon-nucleon collisions per event in $^{19}\text{B} + ^{14}\text{N}$ reactions at 35 and 100 MeV/nucleon, respectively.

cident energy increasing, and the ^{19}B nucleus cannot get enough perturbation to break up into He and Li clusters from the mean field of the ^{14}N target at semi-peripheral collisions in high incident-energy region. With inclusion of nucleon-nucleon collision processes this peak at central collisions disappears due to the reduction by nucleon-nucleon collisions.

We are now able to explain the incident-dependence of the cluster breakup of the ^{19}B nucleus in terms of the competition between the mean-field effect and nucleon-nucleon collisions processes. The mean field from the target causes the cluster breakup of the ^{19}B nucleus, and, on the other hand, nucleon-nucleon collision processes work to destroy

constituent clusters of the ^{19}B nucleus. In low incident-energy region around Fermi energy, the ^{19}B nucleus can get enough perturbation from the mean field of the target to break up into He and Li clusters and they survive with large probability even if nucleon-nucleon collision processes are included. As the incident energy is increasing, the interaction time becomes short, and the mean-field effect becomes weak. As a result, the ^{19}B nucleus is not disturbed by the mean field from the target nucleus enough to break up into He and Li clusters, and the cross section of cluster breakup of the ^{19}B nucleus decreases with the incident energy increasing.

D. Reaction mechanism reflecting the neutron-rich property of the ^{19}B nucleus

Let us move to the subject of the reaction mechanism reflecting the neutron-rich property of the ^{19}B nucleus, which is indicated by production cross sections of fragments with $Z > 5$ as was mentioned previously. The left panel of Fig. 9 displays the excitation functions of C isotopes in $^{19}\text{B} + ^{14}\text{N}$ and $^{13}\text{B} + ^{14}\text{N}$ reactions, which are denoted by solid and broken lines, respectively. The right panel of Fig. 9 shows C-isotope distributions in $^{19}\text{B} + ^{14}\text{N}$ reactions at 35 and 75 MeV/nucleon, which are denoted by solid and broken lines, respectively.

At 35 MeV/nucleon, as is shown in the right panel of Fig. 9, the most abundant C isotope is ^{16}C . Therefore we find that C isotopes are produced by the proton transfer with several neutron emissions. As incident energy is increasing up to 75 MeV/nucleon, the C-isotope distribution shifts to smaller mass region. This means that C isotopes are produced by the proton transfer reaction with more neutron emissions with the incident energy increasing. As is shown in the left panel of Fig. 9, the production cross sections of C isotopes in both ^{19}B and ^{13}B fragmentation decrease with incident energy increasing. This is because large fragments such as a C isotope are hardly produced due to more violent collisions at high incident energy, as was mentioned in the discussion on the fragmentation mechanism reflecting the cluster structure of the ^{19}B nucleus. By comparing ^{19}B fragmentation with ^{13}B fragmentation, the production cross section of C isotopes in

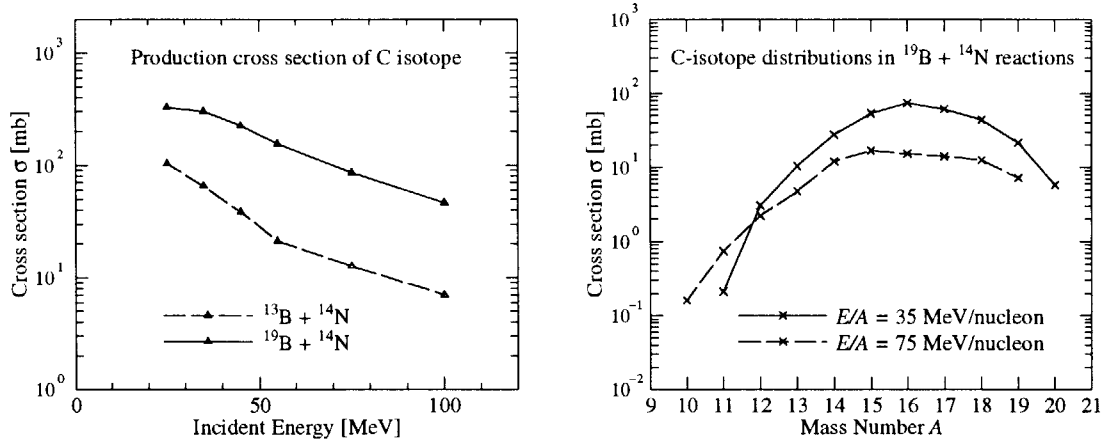


FIG. 9. The top panel shows excitation functions of C isotopes in $^{19}\text{B} + ^{14}\text{N}$ and $^{13}\text{B} + ^{14}\text{N}$ reactions, which are indicated by solid and broken lines, respectively. The bottom panel shows C-isotope distributions in $^{19}\text{B} + ^{14}\text{N}$ reactions at 35 and 100 MeV/nucleon, which are denoted by solid and broken lines, respectively.

^{19}B fragmentation is much larger than that in ^{13}B fragmentation in the whole incident-energy region investigated here. It is expected that, by exchanging neutrons with protons, the ^{19}B nucleus approaches the stability line, and, as a result, the production of C isotopes is more favorable in the ^{19}B induced reaction than in the ^{13}B induced reaction.

There are considered to be two factors arising the abundance of C isotopes in ^{19}B fragmentation compared with in ^{13}B fragmentation. One is that protons of the ^{14}N target feel more attractive potential in the ^{19}B nucleus than in the ^{13}B nucleus. In order to see the dynamical potential for a proton to feel in reactions, we simulate $p + ^{19}\text{B}$ and $p + ^{13}\text{B}$ reactions at 35 MeV without any stochastic collisions and with an impact parameter of 0 fm, and calculate potentials that a proton feels during reactions in the following way. The expectation value of the effective interaction part of Hamiltonian is written as

$$\begin{aligned} \mathcal{V} &= \frac{1}{2} \sum_{ijkl=1}^A \langle \varphi_i \varphi_j | v | \varphi_k \varphi_l - \varphi_l \varphi_k \rangle B_{ki}^{-1} B_{lj}^{-1} \\ &= \sum_i^A E_i \end{aligned} \quad (12)$$

where

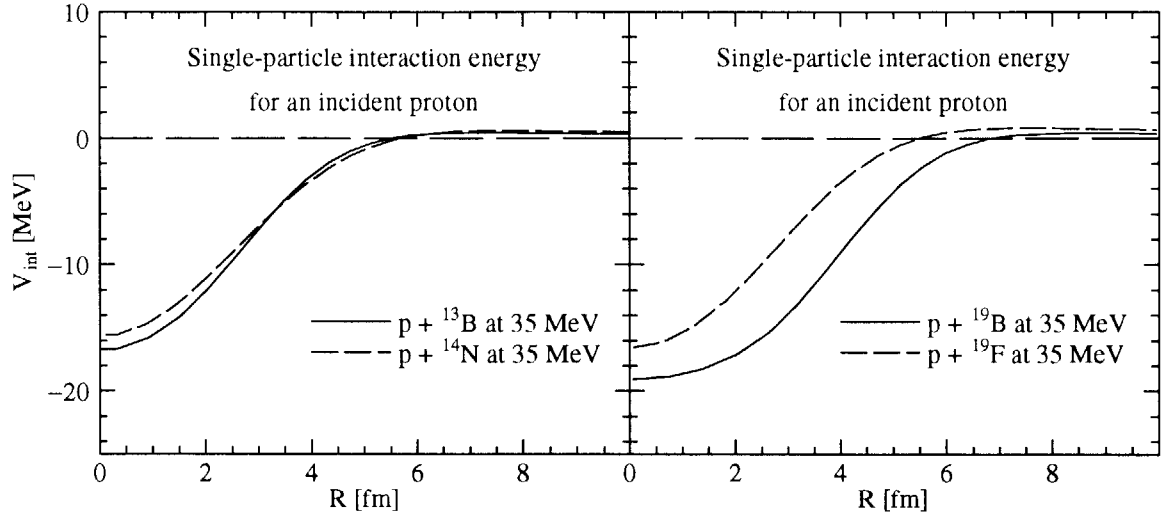


FIG. 10. Potentials that an incident proton feels in $p + {}^{19}\text{B}$ and $p + {}^{13}\text{B}$ reactions at 35 MeV, which are indicated by solid and broken lines, respectively.

$$E_i = \frac{1}{2} \sum_{jkl}^A \langle \varphi_i \varphi_j | v | \varphi_k \varphi_l - \varphi_l \varphi_k \rangle B_{ki}^{-1} B_{lj}^{-1}, \quad (13)$$

and the the Gogny force [18] has the form

$$\begin{aligned} v_{ij} = & \sum_{n=1,2} v_n X_{ij}^{(n)} \exp[-(\mathbf{r}_i - \mathbf{r}_j)^2 / a_n^2] \\ & + v_\rho (1 + P_\sigma) \rho(\mathbf{r}_i)^{1/3} \delta(\mathbf{r}_i - \mathbf{r}_j) \\ X^{(k)} = & W^{(k)} + B^{(k)} P_\sigma - H^{(k)} P_\tau - M^{(k)} P_\sigma P_\tau, \quad k = 1, 2 \end{aligned} \quad (14)$$

Here we define E_i as an interaction energy of i th single particle state [20].

Figure 10 plots E_i , which originates from an incident proton, in $p + {}^{19}\text{B}$ and $p + {}^{13}\text{B}$ reactions at 35 MeV as a function of $R(t)$ instead of time t . Here $R(t)$ is the relative distance at the time t between the centers of mass of a proton and a target nucleus. For the reference, the single-particle interaction energies of an incident proton in the ${}^{19}\text{B}$ and ${}^{13}\text{B}$ target reactions are compared with those in the ${}^{14}\text{N}$ and ${}^{19}\text{F}$ target reactions in left and right panels, respectively. As is obviously seen in Fig. 10, an incident proton feels the most attractive potential in the ${}^{19}\text{B}$ -target reaction among all target reactions calculated here. The depth of the potential that an incident proton feels in the ${}^{19}\text{B}$ nucleus is deeper than that in the normal nucleus, ${}^{19}\text{F}$, due to the neutron-rich property of the ${}^{19}\text{B}$

nucleus, and, on the contrast, the potential of the ^{13}B nucleus is very similar to that of the normal nucleus, ^{14}N and ^{19}F . In addition, the potential of the ^{19}B nucleus has a longer tail compared with that of the ^{19}F nucleus by reflecting the large root-mean-square radius of the ground state of the ^{19}B nucleus, as was shown in the right panel of Fig. 2. Here the root-mean-square-radius of the ground state of the ^{19}F nucleus is 2.83 fm. Another factor for a proton to transfer from the target to the projectile in the AMD framework is nucleon-nucleon collision processes. Since the ^{19}B nucleus has more neutrons than the ^{13}B nucleus, protons in the ^{14}N target collide more frequently with neutrons in the ^{19}B induced reaction compared with in the ^{13}B induced reaction. These two effects are more advantageous to produce C isotopes in ^{19}B fragmentation than in ^{13}B fragmentation. This neutron-rich property of the ^{19}B nucleus is not only a cause of the abundance of C isotopes in ^{19}B fragmentation but also a cause of the contamination of the cluster breakup of the ^{19}B nucleus with the proton transfer in low incident-energy region.

5. SUMMARY AND CONCLUSION

We have investigated incident-energy dependence of the fragmentation mechanism reflecting the cluster structure of the ^{19}B nucleus and the neutron-rich property of the ^{19}B nucleus by calculating the $^{19}\text{B} + ^{14}\text{N}$ and $^{13}\text{B} + ^{14}\text{N}$ reactions at several incident energies with the AMD method. Here the ^{19}B nucleus has the well developed cluster structure, while the ^{13}B nucleus has no seed of clusters in its ground state. We have found that cluster structure of the ^{19}B nucleus in its ground state is reflected as the simultaneous breakup of the ^{19}B nucleus into He and Li isotopes in its fragmentation. This cluster breakup of the ^{19}B nucleus depends on the incident energy, and the contribution of the cluster breakup of the ^{19}B nucleus to the production of Li isotopes is largest around 30 MeV/nucleon. In higher incident-energy region, the cluster structure of the ^{19}B nucleus is not reflected in its fragmentation due to more violent collisions, and, in low incident-energy region, the cluster breakup of the ^{19}B nucleus is contaminated by the breakup of the ^{19}B nucleus accompanied with the proton transfer reaction because of the neutron-

rich property of the ^{19}B nucleus. The neutron-rich property of the ^{19}B nucleus is also reflected in the abundance of the C isotope in ^{19}B fragmentation compared with the ^{13}B fragmentation. A proton feels more attractive potential in the ^{19}B nucleus than in the ^{13}B nucleus, and a proton in the ^{14}N target transfers to the ^{19}B projectile more easily than to the ^{13}B projectile. This proton transfer reaction occurs more easily in lower incident energy because a proton feels an attractive potential for a long time.

This incident-energy dependence is explained in terms of the competition between mean-field effect and nucleon-nucleon collision processes. The mean field from the target makes the ^{19}B nucleus break up into He and Li isotopes, while nucleon-nucleon collision processes work to destroy constituent clusters of the ^{19}B nucleus. In low incident-energy region, the ^{19}B nucleus can get enough perturbation by the mean field from the target to break up into clusters, and these clusters survive from the destructive effect of nucleon-nucleon collision processes. As the incident energy is increasing, the effect of the mean field from the target is weakened because the interaction time becomes short, and the ^{19}B nucleus hardly break up into constituent clusters. As a result, the difference in structure between the ^{19}B and ^{13}B nuclei is not reflected in their fragmentation at high incident energy.

From the above results, we suggest that there is the possibility that the clustering structure of the ^{19}B nucleus may be verified by a coincident experiment between He and Li isotopes in heavy-ion reactions, and that the most suitable incident energy for the experimental verification of the cluster structure of the ^{19}B nucleus is around 30 MeV/nucleon. We also suggest that it may be more advantageous to use a target with large mass because the cluster breakup of the ^{19}B nucleus is caused by the mean field from the target whose effect becomes larger with the mass of the target larger.

However the coincident experiment for the verification of the cluster structure of the ^{19}B nucleus suggested here is hard to be realized in a present situation because the ^{19}B nucleus is the neutron drip-line nucleus, and the intensity of the secondary beam is too weak to perform this kind of experiment. As is shown in Fig. 1, the cluster structure of B isotopes develops with the neutron number increasing. Therefore we must investigate how

sensitive the cluster breakup of B isotopes is to the development of cluster structure in B isotopes, and search for the possibility of the coincident experiment for the verification of the cluster structure of the neutron-rich nucleus by using the ^{17}B beam. Furthermore not only the cluster structure of B isotopes develops, but also the deformation of B isotopes becomes large with the neutron number increasing. Therefore we need perform not only the coincident experiment to verify cluster structure of neutron-rich nuclei but also the γ spectroscopic experiment to verify deformation. These kinds of experiments give us various interesting information for unstable nuclei.

ACKNOWLEDGMENTS

The authors would like to thank H. Sakurai for useful discussions in experiment. Most of computer calculations for this work were performed with the Fujitsu VPP700 at RIKEN, Japan.

References

- [1] *Proceedings of the IV-th International Conference on Radioactive Nuclear Beams, Omiya, Japan, 1996*, ed. S. Kubono, T. Kobayashi and I. Tanihata (Elsevier, 1997), Nucl. Phys. **A616** (1997), Nos. 1,2.
- [2] *Proceedings of the First International Conference on Exotic Nuclei and on Atomic Masses, Arles, France, 1995*, ed. by M. de Saint Simon and O. Sorlin, Edition Frontières (Gif-sur-Yvette, France, 1995).
- [3] *Proceedings of the International Symposium on Physics of Unstable Nuclei, Niigata, 1994*, ed. H. Horiuchi, K. Ikeda, K. Sato, Y. Suzuki and I. Tanihata (Elsevier, 1995), Nucl. Phys. **A588** (1995), No. 1.

- [4] H. Okuno, K. Asahi, H. Ueno, H. Sato, M. Adachi, T. Kubo, T. Nakamura, N. Inabe, A. Yoshida, Y. Ohkubo, T. Ichihara, M. Ishihara, T. Shimoda, H. Miyatake and N. Takahashi, *Hyperfine Interact.* **78**, (1993) 97.
- [5] K. Asahi, H. Ueno, H. Izumi, H. Okuno, K. Nagata, H. Ogawa, Y. Hori, H. Sato, K. Mochinaga, M. Adachi, A. Yoshida, G. Liu, N. Aoi, T. Kubo, M. Ishihara, W. D. Schmidt-Ott, T. Shimoda, H. Miyatake, S. Mituoka and N. Takahashi, in *Proceedings of the International Symposium on Physics of Unstable Nuclei, Niigata, 1994*, ed. H. Horiuchi, K. Ikeda, K. Sato, Y. Suzuki and I. Tanihata.
- [6] M. Seya, M. Kohno and S. Nagata, *Prog. Theor. Phys.* **65** (1981), 204.
- [7] H. Furutani, H. Kanada, T. Kaneko, S. Nagata, H. Nishioka, S. Okabe, S. Saito, T. Sakuda, and M. Seya, *Prog. Theor. Phys. Suppl. No. 68* (1980), 193.
- [8] Y. Kanada-En'yo and H. Horiuchi, *Phys. Rev.* **C52** (1995), 647
- [9] Y. Kanada-En'yo and H. Horiuchi, *Prog. Theor. Phys.* **93** (1995), 115
- [10] A. Ono, H. Horiuchi, T. Maruyama and A. Ohnishi, *Prog. Theor. Phys.* **87** (1992), 1185.
- [11] A. Ono, H. Horiuchi and T. Maruyama, *Phys. Rev.* **C48** (1993), 2946.
- [12] A. Ono and H. Horiuchi, *Phys. Rev.* **C51** (1995), 299.
- [13] E. I. Tanaka, A. Ono, H. Horiuchi, T. Maruyama and A. Engel, *Phys. Rev.* **C52** (1995), 316. A. Engel, E. I. Tanaka, T. Maruyama, A. Ono and H. Horiuchi, *Phys. Rev.* **C52** (1995), 3231.
- [14] *Proceedings of Fifth International Conference on Nucleus-Nucleus Collisions, Taormina, 1994*, ed. M. Di Toro, E. Migneco and P. Piattelli, *Nucl. Phys.* **A583** (1995), 297.
- [15] H. Takemoto, H. Horiuchi, A. Engel and A. Ono, *Phys. Rev.* **C54** (1996), 266.
- [16] H. Takemoto, H. Horiuchi and A. Ono, *Phys. Rev.* **C57** (1998), 811.
- [17] H. Takemoto, H. Horiuchi and A. Ono, *Prog. Theor. Phys.* **101** (1999), 101.

- [18] J. Dechargé and D. Gogny, Phys. Rev. **C21** (1980), 1568.
 [19] M. Saraceno, P. Kramer and F. Fernandez, Nucl. Phys. **A405** (1983), 88.
 [20] A. Tohsaki, Prog. Theor. Phys. **90** (1993), 871.

APPENDIX A: DEFINITION OF NUMBER OF FRAGMENTS

We define the number of fragments N_F as

$$N_F = \sum_{i=1}^A \frac{g(k_i)}{n_i m_i}, \quad (\text{A1})$$

where

$$n_i = \sum_{j=1}^A \hat{f}_{ij}, m_i = \sum_{j=1}^A \frac{1}{n_j} f_{ij}, k_i = \sum_{j=1}^A \bar{f}_{ij} \quad (\text{A2})$$

and

$$\hat{f}_{ij} = F(d_{ij}, \hat{\xi}, \hat{a}), f_{ij} = F(d_{ij}, \xi, a), \bar{f}_{ij} = F(d_{ij}, \bar{\xi}, \bar{a}), \quad (\text{A3})$$

$$d_{ij} = |\text{Re}(\mathbf{Z}_i - \mathbf{Z}_j)|, \quad (\text{A4})$$

$$F(d, \xi, a) = \begin{cases} 1 & \text{if } d \leq a, \\ e^{-2(d-a)^2} & \text{if } d > a. \end{cases} \quad (\text{A5})$$

We have introduced the function

$$g(k) = 1 + g_0 e^{-(k-M)^2/2\sigma^2} \quad (\text{A6})$$

in order to remedy the situation that nuclei around ^{13}B are overbinding in the calculation with the Gogny force. This function should be equal to unity in principle. The parameters used in this paper are listed in Table I.

TABLE I. Parameters in the number of fragments N_F which are used with the Gogny force in this paper.

ξ	a	$\hat{\xi}$	\hat{a}	$\bar{\xi}$	\bar{a}	g_0	σ	M
2.0	0.6	2.0	0.2	1.0	0.5	-0.5	0.25	13.0

APPENDIX B: NUCLEON-NUCLEON CROSS SECTIONS

We use the in-medium nucleon-nucleon cross section $\sigma_{NN} = \min\{\sigma_{NN}^f, \sigma_{NN}^d\}$ as is the same as in Ref. [11]. Here σ_{NN}^f are based on the data of free cross sections and are parameterized as

$$\sigma_{pn}^f = \max\{13335(E/\text{MeV})^{-1.125}, 40\}\text{mb} \quad (\text{B1})$$

$$\sigma_{pp}^f = \sigma_{nn}^f = \max\{4445(E/\text{MeV})^{-1.125}, 25\}\text{mb} \quad (\text{B2})$$

And σ_{NN}^d is the density dependent cross section and is given as

$$\sigma_{pn}^d = \sigma_{pp}^d = \sigma_{nn}^d = \frac{100\text{mb}}{1 + E/(200\text{MeV}) + C\min\{(\rho/\rho_0)^{1/2}, 1\}} \quad (\text{B3})$$

where ρ_0 is the normal density and the parameter C controls the reduction of the cross section due to the medium effect and is taken here $C = 2$. The angular distribution of proton-proton and neutron-neutron collisions is assumed to be isotropic while that of proton-neutron collisions is taken as

$$\frac{d\sigma_{pn}}{d\Omega} \propto 10^{-\alpha(\pi/2 - |\theta - \pi/2|)}, \quad (\text{B4})$$

$$\alpha = \frac{2}{\pi} \max\{0.333\ln[E/(1\text{MeV})] - 1, 0\} \quad (\text{B5})$$

国際単位系 (SI) と換算表

表1 SI基本単位および補助単位

量	名 称	記 号
長 度	メ ー ト ル	m
質 量	キ ロ グ ラ ム	kg
時 間	秒	s
電 流	ア ン ペ ア	A
熱力学温度	ケ ル ビ ン	K
物 質 量	モ ル	mol
光 度	カ ン デ ラ	cd
平 面 角	ラ ジ ア ン	rad
立 体 角	ステラジアン	sr

表3 固有の名称をもつSI組立単位

量	名 称	記号	他のSI単位 による表現
周 波 数	ヘ ル ツ	Hz	s ⁻¹
力	ニ ュ ー ト ン	N	m・kg/s ²
圧 力 , 応 力	パ ス カ ル	Pa	N/m ²
エネルギー, 仕事, 熱量	ジ ュ ー ル	J	N・m
工 率 , 放 射 束	ワ ッ ト	W	J/s
電 気 量 , 電 荷	クー ロ ン	C	A・s
電位, 電圧, 起電力	ボ ル ト	V	W/A
静 電 容 量	ファ ラ ド	F	C/V
電 気 抵 抗	オ ー ム	Ω	V/A
コンダクタンス	ジーメンズ	S	A/V
磁 束	ウ ェ ー バ	Wb	V・s
磁 束 密 度	テ ス ラ	T	Wb/m ²
インダクタンス	ヘ ン リ ー	H	Wb/A
セルシウス温度	セルシウス度	°C	
光 束	ル ー メ ン	lm	cd・sr
照 度	ル ク ス	lx	lm/m ²
放 射 能	ベ ク レ ル	Bq	s ⁻¹
吸 収 線 量	グ レ イ	Gy	J/kg
線 量 等 量	シーベルト	Sv	J/kg

表2 SIと併用される単位

名 称	記 号
分, 時, 日	min, h, d
度, 分, 秒	°, ', "
リットル	L, l
トン	t
電子ボルト	eV
原子質量単位	u
1 eV=1.60218×10 ⁻¹⁹ J	
1 u=1.66054×10 ⁻²⁷ kg	

表5 SI接頭語

倍数	接頭語	記 号
10 ¹⁸	エクサ	E
10 ¹⁵	ペタ	P
10 ¹²	テラ	T
10 ⁹	ギガ	G
10 ⁶	メガ	M
10 ³	キロ	k
10 ²	ヘクト	h
10 ¹	デカ	da
10 ⁻¹	デシ	d
10 ⁻²	センチ	c
10 ⁻³	ミリ	m
10 ⁻⁶	マイクロ	μ
10 ⁻⁹	ナノ	n
10 ⁻¹²	ピコ	p
10 ⁻¹⁵	フェムト	f
10 ⁻¹⁸	アト	a

表4 SIと共に暫定的に維持される単位

名 称	記 号
オングストローム	Å
バー	b
バル	bar
ガリ	Gal
キュリー	Ci
レントゲン	R
ラド	rad
レム	rem

1 Å=0.1nm=10⁻¹⁰m
 1 b=100fm²=10⁻²⁸m²
 1 bar=0.1MPa=10⁵Pa
 1 Gal=1cm/s²=10⁻²m/s²
 1 Ci=3.7×10¹⁰Bq
 1 R=2.58×10⁻⁴C/kg
 1 rad=1cGy=10⁻²Gy
 1 rem=1cSv=10⁻²Sv

(注)

- 表1-5は「国際単位系」第5版、国際度量衡局1985年刊行による。ただし、1 eV および 1 u の値はCODATAの1986年推奨値によった。
- 表4には海里、ノット、アール、ヘクタールも含まれているが日常の単位なのでここでは省略した。
- bar は、JISでは流体の圧力を表す場合に限り表2のカテゴリーに分類されている。
- E C閣僚理事会指令では bar, barn および「血圧の単位」mmHgを表2のカテゴリーに入れている。

換 算 表

力	N (=10 ⁵ dyn)	kgf	lbf
	1	0.101972	0.224809
	9.80665	1	2.20462
	4.44822	0.453592	1

粘 度 1 Pa・s (N・s/m²)=10 P (ポアズ)(g/(cm・s))

動粘度 1 m²/s=10⁶St (ストークス)(cm²/s)

圧	MPa (=10bar)	kgf/cm ²	atm	mmHg (Torr)	lbf/in ² (psi)
	1	10.1972	9.86923	7.50062×10 ²	145.038
力	0.0980665	1	0.967841	735.559	14.2233
	0.101325	1.03323	1	760	14.6959
	1.33322×10 ⁻¹	1.35951×10 ⁻²	1.31579×10 ⁻³	1	1.93368×10 ⁻²
	6.89476×10 ⁻²	7.03070×10 ⁻³	6.80460×10 ⁻²	51.7149	1

エネルギー・仕事・熱量	J (=10 ⁷ erg)	kgf・m	kW・h	cal (計量法)	Btu	ft・lbf	eV
	1	0.101972	2.77778×10 ⁻⁷	0.238889	9.47813×10 ⁻⁴	0.737562	6.24150×10 ¹⁸
	9.80665	1	2.72407×10 ⁻⁶	2.34270	9.29487×10 ⁻³	7.23301	6.12082×10 ¹⁹
	3.6×10 ⁶	3.67098×10 ⁵	1	8.59999×10 ⁵	3.11213	2.65522×10 ⁶	2.24694×10 ²⁵
	4.18605	0.426858	1.16279×10 ⁻⁶	1	3.96739×10 ⁻³	3.08747	2.61272×10 ¹⁹
	1055.06	107.586	2.93072×10 ⁻⁴	252.042	1	778.172	6.58515×10 ²¹
	1.35582	0.138255	3.76616×10 ⁻⁷	0.323890	1.28506×10 ⁻³	1	8.46233×10 ¹⁸
	1.60218×10 ⁻¹⁹	1.63377×10 ⁻²⁰	4.45050×10 ⁻²⁶	3.82743×10 ⁻²⁰	1.51857×10 ⁻²²	1.18171×10 ⁻¹⁶	1

1 cal= 4.18605J (計量法)
 = 4.184J (熱化学)
 = 4.1855J (15°C)
 = 4.1868J (国際蒸気表)
 仕事率 1 PS (仏馬力)
 = 75 kgf・m/s
 = 735.499W

放射能	Bq	Ci
	1	2.70270×10 ⁻¹¹
	3.7×10 ¹⁰	1

吸収線量	Gy	rad
	1	100
	0.01	1

照射線量	C/kg	R
	1	3876
	2.58×10 ⁻⁴	1

線量当量	Sv	rem
	1	100
	0.01	1

Incident-energy Dependence of the Fragmentation Mechanism Reflecting the Clustering Structure of the ^{19}B Nucleus

[Redacted text block]